Received: 23 May 2023 | Revised: 22 November 2023 | Accepted: 10 December 2023

DOI: 10.1002/wat2.1712

ADVANCED REVIEW

WIREs WATER WILEY

A review of atmospheric water vapor lidar calibration methods

Xinqian Guo[1,2] | Decheng Wu[1,2] | Zhenzhu Wang[1,2] | Bangxin Wang[1,2] | Cheng Li[1,2] | Qian Deng[1,2] | Dong Liu[1,2,3]

[1]Key Laboratory of Atmospheric Optics, Anhui Institute of Optics and Fine Mechanics, Hefei Institutes of Physical Science, Chinese Academy of Sciences, Hefei, China

[2]Advanced Laser Technology Laboratory of Anhui Province, Hefei, China

[3]Wan Jiang New Industry Technology Development Center, Tongling, China

Correspondence
Dong Liu, Key Laboratory of Atmospheric Optics, Anhui Institute of Optics and Fine Mechanics, Hefei Institutes of Physical Science, Chinese Academy of Sciences, Hefei, 230031, China.
Email: dliu@aiofm.cas.cn

Funding information
Hefei Research Institute Dean Fund Top Talents Cultivation Project, Grant/Award Number: BJPY2021A03; the Open Fund of 'Anhui Meteorological Detection Equipment Engineering Technology Research Center', Grant/Award Number: 2023QXTC05; the National Key R&D Program of China, Grant/Award Number: 2018YFB0504500; the Young Scientists Fund of the National Natural Science Foundation of China, Grant/Award Number: 42305142; the Natural Science Foundation of Anhui Province, Grant/Award Number: 2208085UQ01; the Key Collaborative Research Program of the Alliance of International Science Organizations, Grant/Award Number: ANSO-CR-KP-2020-09; the HFIPS Director's Fund, Grant/Award Number: YZJJ202205-CX

Edited by: Thom Bogaard, Associate Editor, Jan Seibert, Senior Editor, and Wendy Jepson, Editor-in-Chief

Abstract

Atmospheric water vapor is a crucial factor in the Earth's water cycle. As an important greenhouse gas, changes in the spatio-temporal distribution of atmospheric water vapor can contribute to the occurrence of various extreme weather phenomena. Lidar, with its high spatial and temporal resolutions, has great potential for applications in water vapor profile detection. Raman lidar and differential absorption lidar (DIAL) have been successfully used to detect atmospheric water vapor. System calibration is crucial to ensure that the measured profile accurately represents the concentration profile of atmospheric water vapor. Choosing an effective system calibration method can ensure the accuracy of long-term lidar measurements. This paper reviews the latest progress and applications of atmospheric water vapor lidar calibration in recent years. The basic principles of Raman lidar and DIAL calibration are introduced. Various methods and benefits of system calibration are discussed. Raman lidar has three commonly used calibration methods: external calibration, internal calibration, and hybrid calibration methods. The most commonly used method is external calibration based on radiosondes. DIAL is usually implemented with an advantageous self-calibration method. Finally, potential development directions for atmospheric water vapor lidar and calibration technology are discussed.

This article is categorized under:

Science of Water > Methods

Engineering Water > Methods

Human Water > Value of Water

KEYWORDS

atmospheric water vapor, differential absorption lidar (DIAL), lidar system calibration, Raman lidar

1 | INTRODUCTION

Water vapor, as the foundation of life on Earth, plays a dominant role in the atmospheric water cycle, which is essential for supporting life on our planet. Additionally, it is a crucial component of atmospheric chemistry. Because it effectively absorbs and emits infrared radiation, it causes fluctuations in near-ground temperature, which in turn affects water vapor concentrations. Changes in water vapor concentration strongly affect both anthropogenic and natural climate responses (Lu et al., 2018; Shine & Sinha, 1991). In recent decades, there has been an increase in extreme precipitation events, leading to catastrophic floods or droughts. This poses a significant threat to human livelihoods and well-being. Extreme precipitation and its associated hazards (e.g., floods, lightning, etc.) are directly influenced by atmospheric water vapor concentrations (Mazany et al., 2002). Additionally, it contributes to global warming. In the atmosphere, unlike CO_2, the amount of water vapor directly impacts the surface air temperature. The greenhouse effect system has the greatest positive feedback, where high temperatures lead to an increase in water vapor. These increase in water vapor, in turn, causes a further rise in temperatures. The water vapor spatial distribution of water vapor is highly irregular, and its concentration varies due to several factors, including season, time of day, location, and altitude. Atmospheric water vapor detection with high spatial and temporal resolution is of great significance (He et al., 2022). Because its concentration is small and the spatio-temporal distribution of concentration is irregular and changes rapidly, the atmospheric water vapor has always been a challenging parameter to accurately measure. Radiosonde, as the commonly used in situ detection method, is limited by its poor temporal and spatial resolution (Guichard et al., 2000). Meteorological towers can directly obtain data with high accuracy and high temporal resolution (Sandeep et al., 2015). However, their measurement range is limited by the height of the towers, making it difficult to capture data from the entire boundary layer. Microwave radiometers, another commonly used method for detecting atmospheric water vapor, can provide high temporal resolution. However, their spatial resolution is low, especially for upper water vapor measurements, and they are vulnerable to interference from clouds and rainfall (Pérez-Ramírez et al., 2014). Active remote sensors, such as lidar, have become popular for their ability to detect atmospheric water vapor with high spatio-temporal resolutions. Raman lidar and differential absorption lidar (DIAL) are commonly employed to detect atmospheric water vapor.

Raman scattering lidar obtains the concentration of the gas to be measured by collecting the Raman scattering signal of the gas molecule of interest and the reference gas molecules (usually nitrogen and oxygen). Raman scattering by atmospheric water vapor was first observed in 1969 (Melfi et al., 1969). Later, Cooney successfully employed Raman lidar to detect vertical water vapor profiles, which demonstrated the suitability of Raman lidar for water vapor detection (Cooney, 1969). With its low requirements for spectral resolution, Raman lidar has been widely applied by research institutes in the past few decades. However, the Raman scattering cross-sections of water vapor molecules are very small, resulting in a low signal-to-noise ratio of the lidar echo signal. This limitation restricts its application during the daytime. Therefore, Raman lidar was mainly utilized at night-time for a long time. With the rapid development of high-energy lasers and narrow-band optical filter technology in recent years, it has become possible to effectively avoid the influence of daylight background. Daytime detection by Raman lidar has been achieved by some researchers, but it is costly (Chazette et al., 2014). However, the signal measured by Raman lidar is a profile that is proportional to the mixing ratio. Therefore, careful and regular system calibration is necessary (Spuler et al., 2015). Calibration can effectively eliminate systematic errors caused by uncertainties in Raman cross-section and instrumental factors, including transmittance of optics, quantum efficiency and gain of detectors, and average atmospheric transmittance.

In 1966, Schotland first proposed the DIAL to measure atmospheric water vapor at the Fourth Conference on Remote Sensing of the Environment. DIAL has been developed and matured since the 1970s. The DIAL for detecting atmospheric water vapor takes advantage of the fact that water vapor molecules absorb wavelengths that are close to each other with varying intensities. Depending on the chosen reflector, it can detect the columnar concentration and height distribution of atmospheric water vapor content. The DIAL detection accuracy is comparable to Raman lidar and has the advantage of being able to detect during the daytime (Wulfmeyer & Bösenberg, 1998). Many typical DIAL applications for ground-based and airborne platforms have emerged (Bruneau et al., 2001; Fix et al., 2010; Späth et al., 2016). NASA's airborne lidar test system has successfully obtained water vapor profiles and studied their characteristics. They have completed the testing using semiconductor lasers and are now implementing commercial applications. In addition, due to its self-calibration capability (described in detail in the next section), the DIAL does not need complex calibration devices like the Raman lidar. Instead, it only obtains the absorption cross-section corresponding to the detection wavelength. Calibration is still an integral part of the DIAL system. System calibration of DIAL translates into the problem of how to accurately obtain the absorption cross-section.

Like every other precision instrument, calibration is a crucial step for radars to provide the accurate information. General radar calibration enables the radar to accurately measure the position, distance, and other relevant parameters of an object. The principles of general radar calibration are as follows: (1) Calibration should be based on traceable standards or references to ensure confidence and repeatability of calibration results. (2) To ensure the accuracy and consistency of the radar system, calibration parameters should remain stable over a longer period of time. Calibration parameters should be regularly checked and maintained to account for factors such as environmental changes and equipment aging. (3) Calibration should minimize errors and improve the accuracy of water vapor detection lidar measurements. (4) To determine the accuracy and margin of error of calibration results, it is necessary to validate the accuracy and reliability of the calibration process. (5) The calibration process and results should be documented in detail and accurately. These records are important for future inspection, calibration, and traceability. For atmospheric water vapor detection lidar, the calibration principle not only follows the general radar calibration principle. In addition, (1) the interaction characteristics (scattering and absorption) between the laser and the water vapor molecules need to be considered. (2) It is necessary to choose a calibration method with high spatiotemporal resolution. System calibration of lidar is important, and many researchers have presented methods to promote accurate and stable measurements of water vapor over long periods. In this review, we introduce the necessity and measurement methods of atmospheric water vapor. This paper focuses on Raman lidar and the DIAL. The principles of lidar system and calibration are summarized, and the approaches to calibrate the system are given. Finally, we introduce the practical applications of atmospheric water vapor lidar technology and its potential areas for future development.

2 | THEORY OF WATER VAPOR DETECTION LIDAR

2.1 | Raman lidar

The scattering of atmospheric molecules involves both elastic and inelastic processes. Elastic scattering (such as Rayleigh scattering, and Mie scattering) means the scattered photon and the incident photon have the same frequency as depicted by the green line in Figure 1. Inelastic scattering (such as Raman) leads to the molecule's quantum state change and the frequency of the scattered photon shifts as the red line in Figure 1. The frequency shift $\Delta\nu = \Delta E/\mathrm{hc}$ is determined by the molecular species, enabling qualitative identification of atmospheric water vapor. In the equation, ΔE, h, and c represent the difference of the specific molecular energy levels, Planck's constant, and the light speed in a vacuum, respectively. The energy difference of the specific molecule can be calculated. Based on weak inelastic scattering, Raman lidar obtains water vapor concentration by the magnitude of the Raman scatter echo signal. An inelastic scattering effect called Raman scattering occurs when the laser passes through atmospheric molecules, which is independent of the incident laser frequency. The Raman frequency shift of molecules is only related to the molecular species, and the scattering intensity is proportional to the molecular concentration, so the atmospheric water vapor concentration profile can be back-performed based on the intensity of the Raman scattering signal.

Usually, Raman lidar obtains the water vapor concentration by measuring the scattered signals of water vapor molecules and N_2 molecules (or O_2 molecules) in the atmosphere. This is because the content of nitrogen (or oxygen) in the atmosphere remains relatively stable, and a significant amount of nitrogen (or oxygen) in the atmosphere helps to reduce the atmospheric attenuation in the calculation equation.

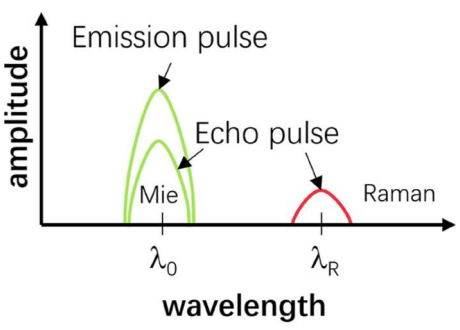

FIGURE 1 The principle of Raman lidar.

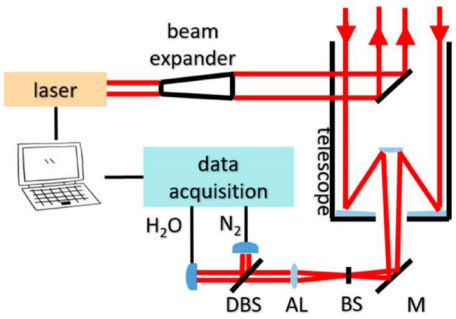

FIGURE 2 Typical setup of water vapor Raman lidar. AL, achromatic lens; BS, beam shutter; M, mirror.

The typical setup of a water vapor Raman lidar is shown in Figure 2. The emission unit consists of a computer-controlled laser, beam expander, and reflector. This part is used to enhance the cross-section of the laser beam and increase the transmission distance. The receiving unit consists of the telescope, reflector mirror, beam shutter, and achromatic lens. The receiving unit receives the scattered signal and transmits the collected light signal to the detection and acquisition unit. The detector, data acquisition card, and computer form the data detection and acquisition processing unit. This unit converts the collected signal into an electrical signal. The conversion process should take into account the saturation of the detector and ensure that the electrical signal is transmitted to the computer without any abnormalities.

The background signal received by a detector in Raman lidar can be expressed as (Whiteman, 2003a):

$$P(\Delta\lambda_X, r) = \frac{O_X(r)F_X(T)P_0(\lambda_L)AN_X(r)[\mathrm{d}\sigma_X(\pi)/\mathrm{d}\Omega]\xi(\lambda_X)}{r^2}\exp\left\{-\int_0^r[\alpha(\lambda_L, r') + \alpha(\lambda_X, r')]dr'\right\} \tag{1}$$

where $P_0(\lambda_L)$, $O_X(r)$, and $F_X(T)$ are the laser output power at λ_L, the overlap function, and the temperature-dependent function, respectively. A expresses receiver-telescope area, $N_X(r)$, $\mathrm{d}\sigma_X(\pi)/\mathrm{d}\Omega$, and $\xi(\lambda_X)$ are the number density of X molecular, pertinent Raman backscatter cross-section, and lidar system's transmission efficiency, respectively. $\alpha(\lambda_L,r')$ and $\alpha(\lambda_X,r')$ are extinction coefficients.

2.1.1 | WVMR

The water vapor mixing ratio (WVMR) is the mass ratio of water vapor in humid air to dry air (Whiteman, 2003b).

$$\omega(r) = \frac{\mathrm{MW}_{\mathrm{H_2O}}}{\mathrm{MW}_{\mathrm{DryAir}}(r)}\frac{N_H(r)}{N_{\mathrm{DryAir}}(r)} \cong \frac{\mathrm{MW}_{\mathrm{H_2O}}}{\mathrm{MW}_{\mathrm{DryAir}}(r)}\frac{0.78N_H(r)}{N_N(r)} \cong 0.485\frac{N_H(r)}{N_N(r)} \tag{2}$$

where ω means the WVMR. $\mathrm{MW}_{\mathrm{H_2O}}$ and $\mathrm{MW}_{\mathrm{DryAir}}$ are the relative molecular mass of water vapor and dry air, respectively. In the lower atmosphere, the ratio of nitrogen to dry air is nearly constant (~0.78). So the density of dry air (N_{Dryair}) can be replaced by the density of nitrogen (N_N/0.78). The WVMR can be expressed as the H_2O and N_2 mixing ratio divided by 0.78. The ratio of the Raman lidar detections of the H_2O and N_2 can be expressed as (including temperature sensitivity):

$$\frac{P(\Delta\lambda_H, r)}{P(\Delta\lambda_N, r)} = \frac{O_H(r)F_H[T(r)]N_H(r)[\mathrm{d}\sigma_H(\pi)/\mathrm{d}\Omega]\xi(\lambda_H)}{O_N(r)F_N[T(r)]N_N(\mathrm{r})[\mathrm{d}\sigma_N(\pi)/\mathrm{d}\Omega]\xi(\lambda_N)}\exp\left\{-\int_0^r[\alpha(\lambda_H, r') - \alpha(\lambda_N, r')]dr'\right\} \tag{3}$$

it can be seen that

$$\omega = k\frac{O_N(r)F_N[T(r)]P(\lambda_H, r)[\mathrm{d}\sigma_N(\pi)/\mathrm{d}\Omega]\xi(\lambda_N)}{O_H(r)F_H[T(r)]P(\lambda_N, r)[\mathrm{d}\sigma_H(\pi)/\mathrm{d}\Omega]\xi(\lambda_H)}\exp\left\{-\int_0^r[\alpha(\lambda_N, r') - \alpha(\lambda_H, r')]dr'\right\} \tag{4}$$

in the Equation (2) k(~0.485) represents the constant of proportionality.

For an ideal lidar system, the ratio of $O_N(r)/O_H(r)$ remains constant across the measurement range.

$$\omega = k^* \frac{F_N[T(r)]P(\lambda_H, r)}{F_H[T(r)]P(\lambda_N, r)} \exp\left\{-\int_0^r [\alpha(\lambda_N, r') - \alpha(\lambda_H, r')]dr'\right\} \tag{5}$$

$$k^* = 0.485 \frac{O_N(r)[d\sigma_N(\pi)/d\Omega]\xi(\lambda_N)}{O_H(r)[d\sigma_H(\pi)/d\Omega]\xi(\lambda_H)} \tag{6}$$

where k* indicates the calibration factor of the lidar system. To realize the high accuracy and stable operation of the lidar, careful and regular calibration of the system is essential. The $F_N[T(r)]/F_H[T(r)]$ means temperature-dependent ratio, always appearing as a constant multiplier in the equation when the temperature can be neglected (Ansmann et al., 1992; Whiteman et al., 1992).

2.2 | DIAL

DIAL takes advantage of the differences in the characteristic absorption spectra of different molecules in the atmosphere to qualitatively identify water vapor in the atmosphere. Normally, DIAL uses two laser wavelengths close to the absorption peak and absorption valley of the same molecule. These two wavelengths have a small wavelength separation. One at the absorption peak, which will be strongly absorbed by the gas being measured, is called online. The other is located in the absorption valley, where absorption is minimal and it is called offline. The wavelength online is marked as λ_{on}, at offline is marked as λ_{off} as shown in Figure 3. The scatter echo signal of DIAL is based on the scattering of aerosol particles and is generated by elastic scattering. Since the wavelengths of the two laser beams are closely spaced, it can be assumed that other substances in the atmosphere, as well as the transmitter, and receiver, have almost the same effect on the two beams. By using the difference between the returned signals of the two beams, the interference

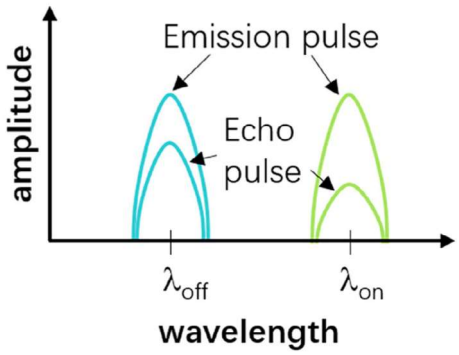

FIGURE 3 The principle of dual-wavelength differential absorption lidar.

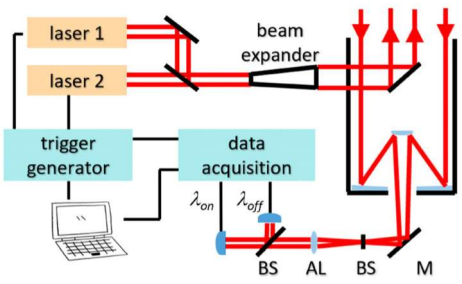

FIGURE 4 (a) Typical setup of water vapor DIAL. λ_{on}: online channel; λ_{off}: offline channel; AL, achromatic lens; BS, beam splitter; M, mirror.

term can be eliminated. The distribution of water vapor is determined by measuring the change in water vapor absorption at two different wavelengths as height increases (Weitkamp, 2006).

As shown in Figure 4, the setup of DIAL is similar to that of a Raman lidar, with the exception that it requires two lasers to be emitted into the atmosphere at separate online and offline wavelengths. DIAL uses the numerous aerosol particles present in the surrounding atmosphere as scatterers. By measuring the concentration of gas molecules at various distances along the laser transmission path, the spatial distribution of the molecular concentration of the target gas can be obtained. DIAL determines water vapor concentration based on the magnitude of the difference in scattering echo signals at λ_{on} and λ_{off}.

The principle of DIAL is based on the elastic backscatter lidar equation (Collis & Russell, 1976):

$$P(\nu,R) = O_X(r)P_0\left(\frac{A}{R^2}\right)\left(\frac{c\tau_L}{2}\right)\eta(\nu,R)\beta(\nu,R)\exp\left[-2\int_0^R \alpha(r)dr\right] \tag{7}$$

where $P(\nu,R)$ and P_0 are the power received at distance R and laser output power, respectively. $O_X(r)$, means the overlap function. $\eta(\nu,R)$, A, c, τ_L, β, and α are the efficiency of the receiver, the area of the telescope, the light speed, the duration of the laser pulse, the backscatter coefficient, and the extinction coefficient of atmospheric, respectively.

DIAL operates at two wavelengths where the interested gas has an absorption difference. Define P_{off} and P_{on} represent the lidar echo signal at the almost no absorption wavelength λ_{off} and strongly absorbing wavelength λ_{on}, respectively. The difference $\Delta\alpha = N\Delta\sigma$. $\sigma(\nu,r)$ is the absorption cross-section, $N(r)$ is molecular number density.

$$N = \frac{1}{2\Delta\sigma}\left[\frac{d}{dR}\ln\frac{P_{off}}{P_{on}}\right] \tag{8}$$

The equation states that all instrument constants can be eliminated by mathematical calculations and that the gas concentration is only related to the lidar signal and differential absorption cross-section. Thus, for DIAL measurements, the system can self-calibrate. Only the absorption differential cross-section at λ_{on} and λ_{off} wavelengths needs to be known (Bruneau et al., 2001).

3 | SYSTEM CALIBRATION

3.1 | Calibration of Raman lidar

Several methods have been developed for Raman lidar calibration in recent years, such as external methods, internal methods, and a hybrid of internal and external methods.

3.1.1 | External calibration method

The most common technique is to compare it with other water vapor measurement techniques to obtain system constants. Instead of determining the coefficients for each component of the lidar system and without assessing the uncertainty of the Raman cross-section, this method directly calibrates the entire system. The advantage of this technique is that it is not necessary to know the transfer function of the lidar for both two channels nor is it necessary to know the Raman cross-sections of N_2 and water vapor. An external measurement is easy to implement.

A typical external reference instrument is a mereological radiosonde, as it provides vertical information on water vapor (Adam et al., 2010; Ansmann et al., 1992; David et al., 2017; Dirksen et al., 2014; Ferrare et al., 1995; Hicks-Jalali et al., 2018; Kulla & Ritter, 2019; Madonna et al., 2011; Mattis et al., 2002; Melfi, 1972; Miloshevich et al., 2009; Moss et al., 2013; Whiteman et al., 1992; Whiteman, Russo, et al., 2006). Radiosonde, with its high vertical resolution detection potential and real-time monitoring capabilities, has been the benchmark method for measuring atmospheric water vapor for decades (Pérez-Ramírez et al., 2014). Raman lidar signals were first reported for comparison with nearly coincident balloon-sonde measurements in 1972. As shown in Figure 5, by comparing the Raman signal V_{H_2O}/V_{N_2} with the balloon-sonde measurement by weighted least squares fitting, the functional relationship between the Raman scattering

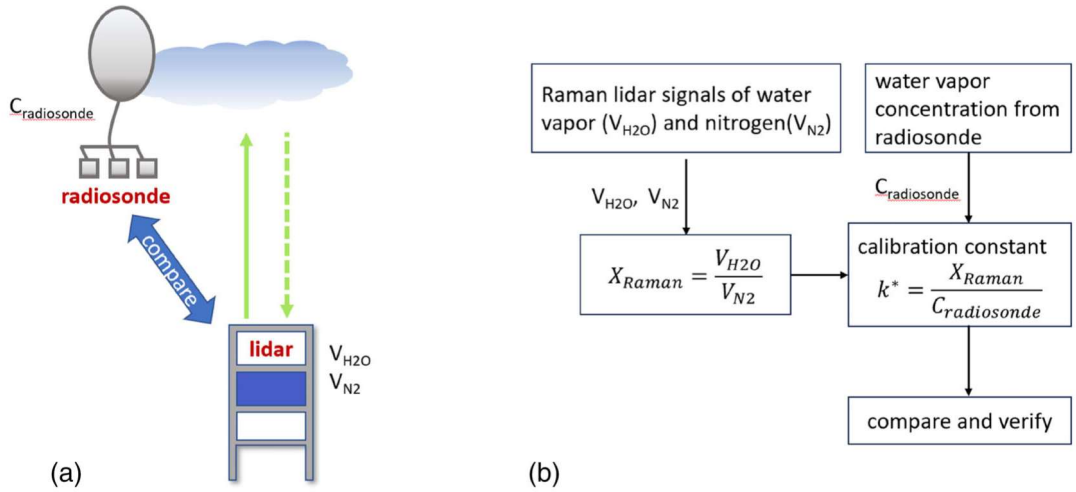

FIGURE 5 (a) Diagram of radiosonde-based calibration; (b) Radiosonde-based calibration process.

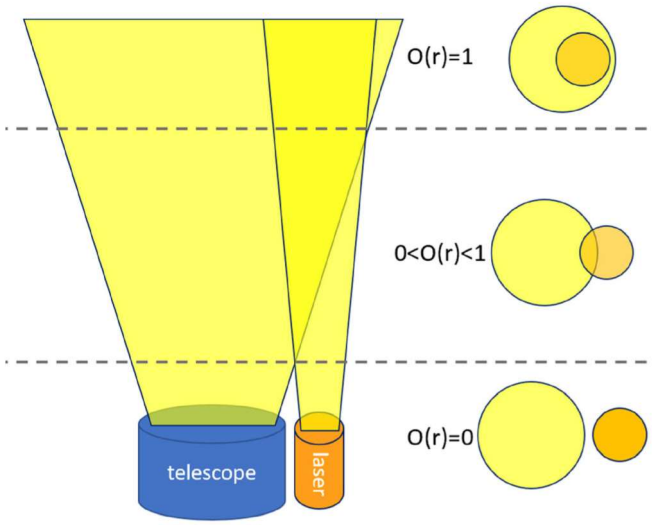

FIGURE 6 Diagram of the overlap near the lidar system.

signal and the balloon-sonde signal was obtained (Melfi, 1972). A few years later, in 1987, the lidar data was compared with a radiosonde from the same period using a single calibration constant. The result indicated the lidar and the balloon detection results were in good agreement (Whiteman et al., 1992). In addition, the calibration stability of different radiosondes was compared. During the1991 and 1993, a comparison of NASA/GSFC Raman lidar and radiosondes measurements showed that the lidar water vapor profiles calibrated with AIR radiosonde were 3%– 5% higher than that calibrated by the Vaisala radiosonde (Ferrare et al., 1995).

After decades of development, the RS92 has become the most commonly used radiosonde. The literature indicates that the relative humidity uncertainty of radiosondes is from 5% to 15%, depending on the launch time (Dirksen et al., 2014; Miloshevich et al., 2009). It is difficult to accurately model radiosondes for achieving precise humidity measurements. To minimize the calibration uncertainty caused by RS92 reference deviation, the GCOS (Global Climate Observing System) Reference Upper-Air Network (GRUAN) developed a specific correction function for the Vaisala RS92 radiosondes (Immler et al., 2010; Seidel et al., 2009). The results showed a 2% reduction in relative humidity error for GRUAN RS92 (Dirksen et al., 2014).

Despite their great advantages, radiosondes suffered from many uncertainties such as poor temporal resolution (two to four launches per day) (Turner et al., 2003), low horizontal resolution (heavy and costly apparatus, a flight exclusion area, far distance several 100 km apart from each other between sites), the long time to ascend (~30 min) (Hicks-Jalali

et al., 2018), the dependence of temperature (Miloshevich et al., 2004), and the batch dependence of calibration (Turner et al., 2003). Additionally, especially in windy weather, they can drift and may not always remain in the same position as the lidar. The homogeneity of WVMR in the troposphere is generally good, and this problem can be ignored. But in planetary boundary layers, especially near coastal regions or mountainous areas, they are poorly homogeneous. These sources of uncertainty need to be characterized and corrected, if possible.

To resolve the measurement differences between radiosondes and Raman lidar, and to explore innovative approaches for enhancing the absolute accuracy of those water vapor equipment, in October–November 2003, a project called the AIRS Water Vapor Experiment-Ground (AWEX-G) was held (Whiteman, Russo, et al., 2006). There is a partial overlap between the laser transmitter and the receiver, especially near the system. As shown in Figure 6, there is a nonlinear relationship between the received power of the receiver and the concentration of the gas, which makes it difficult to perform high-precision calculations. Therefore, the overlap function of the lidar can be corrected by comparing the water vapor data measured by Raman lidar and radiosonde to generate an average overlap correction factor (Ferrare et al., 2004; Whiteman, Demoz, et al., 2006). The corrections were employed for all Raman lidar during AWEX-G. As a result of this overlap correction for AWEX-G, the system calibration factor is reduced by approximately 5%.

Due to the temperature dependence of Raman spectroscopy, there are significant differences in atmospheric temperature in different regions at different altitudes (Whiteman, 2003a). The effective cross-section will change significantly with temperature, which will affect the detection results. The temperature correction technique was employed and analyzed in the literature (Whiteman, 2003b). The ratio $F_N(T)/F_H(T)$ represents the complete temperature dependence of Raman lidar detection. $F_N(T)$ and $F_H(T)$ are the temperature dependence functions of Raman lidar measurements of nitrogen and water vapor, respectively (Whiteman, Demoz, et al., 2006). During AWEX-G, the Raman lidar signal was acquired during radiosonde launches. The temperature measured by the radiosonde can be used to calculate the ratio $F_N(T)/F_H(T)$ of each Raman lidar. The results showed that the temperature-corrected standard deviation at any altitude is 1% smaller than the maximum standard deviation that exists in the boundary layer. In addition, the water vapor line with a central wavelength of 407.45 nm is not sensitive to temperature changes (Whiteman, Demoz, et al., 2006). For the choice of 407.45 nm for water vapor detection, the temperature correction is not required.

To study the impact of temperature and humidity on the performance of lidar and radiosonde, Adam et al. (2010) examined the correlation between their relative performance in different atmospheric conditions, particularly when they exhibited poor agreement. They developed a grid based on temperature-relative humidity spatial analysis, analyzed the lidar-radiosonde coherence, and identified regions of interest for different correlations as a regular of altitude, temperature, or humidity. The results showed that the water vapor retrieved by the Atmospheric Infrared Sounder and Tropospheric Emission Sounder satellite is basically consistent with the comparison trend of the Howard University calibrated Raman lidar.

For any external calibration, the varying fields of view of the lidar and the other detection devices will introduce additional uncertainty in the calibration process. For the calibration by the radiosonde, this location problem can be particularly challenging. It takes about 30 minutes for radiosondes to reach the tropopause. During this time, the radiosonde may move far away from the lidar. If the detected air mass is horizontally homogeneous, the distance that the radiosonde traveled away normally has little to do with the calibration measurement. However, if we happen to calibrate at the edge of the air mass or if the air mass is completely inhomogeneous in the horizontal direction, the water vapor field may vary significantly as the radiosonde travels different distances. In order to bring different devices to a common location for comparison with each other and to resolve measurement discrepancies, AWEX-G was held in the fall of 2003 (Whiteman, Russo, et al., 2006). In addition, Leblanc and Mcdermid presented the "radiosonde-tracking" technique, which combined the absolute calibration of the radiosonde with the (non-motion) calibration of a standard lamp (detailed in 3.1.2 hybrid methods) (Leblanc & McDermid, 2008).

In 2018, Hicks-Jalali et al. (2018) focused on the co-location problem and solved it using a trajectory technique. To ensure consistent quality in the test area for both the lidar and the radiosonde, the trajectory calibration technique matched each altitude measurement value of the lidar with the corresponding radiosonde data. This ensured the calibration process was as accurate as possible. The calibration integration time, which considered the homogeneous area surrounding the lidar, varied depending on the during that the radiosonde remained within the homogeneous region. The flowchart in Figure 7 illustrates the steps of the novel trajectory calibration. Finally, they demonstrated this improved calibration technique using the GRUAN RS92 and the Meteo Swiss Raman Lidar for Meteorological Observation (RALMO). The results show that the average uncertainty for radiosondes is about 4%.

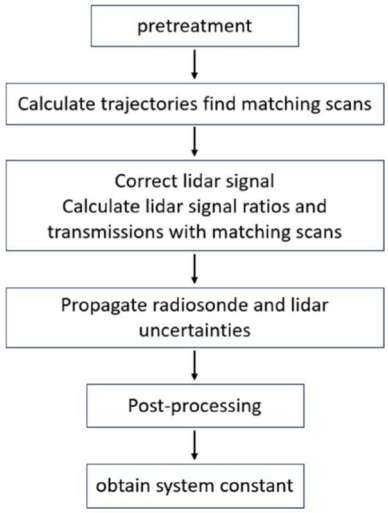

FIGURE 7 Flowchart of the calibration steps by the Trajectory Method (Hicks-Jalali et al., 2018). Pretreatment includes filter scans for clouds, interpolating radiosonde onto the lidar grid, and defining a 3 km homogeneous cylinder. Post-processing including limit calibration range, smooth lidar, and radiosonde find correction regions.

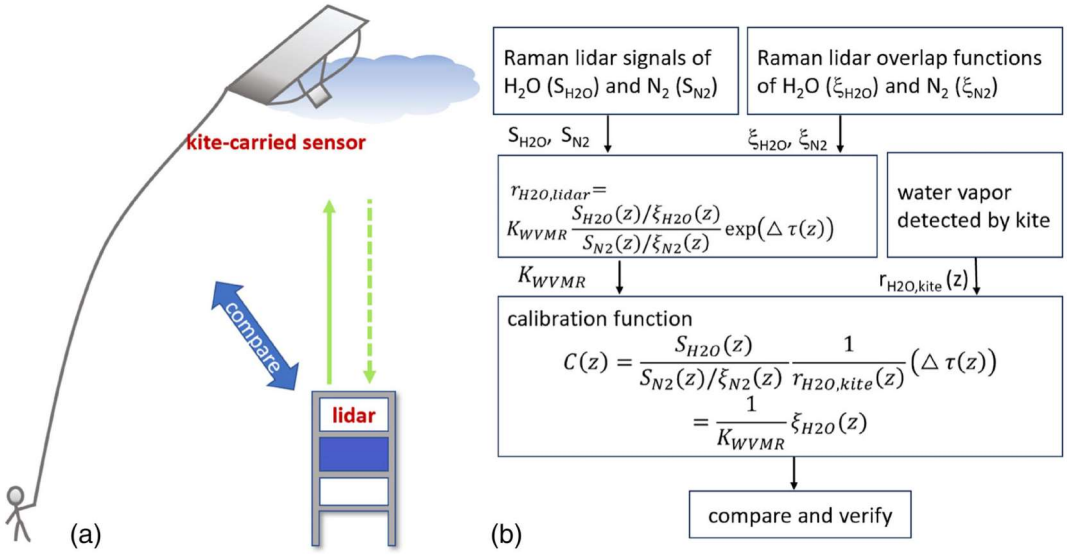

FIGURE 8 (a) Diagram of kite-carried sensor calibration; (b) Results of lidar calibration by kite-carried humidity sensor (Totems & Chazette, 2016).

There are several different calibration processes for water vapor detection using Raman lidar, such as the use of a kite-borne meteorological probe (Reiche et al., 2012; Totems & Chazette, 2016). Similar to the calibration based on a radiosonde, the calibration constant is divided by the water vapor data of a kite-based atmospheric sounding system is divided by the water vapor data from the Raman lidar. Kite-borne atmospheric detection has a long history, which started with the France "meteorographs" in 1898. Kites have an impressive detection altitude range and advancements in materials and fabrics have made them lighter, cheaper, and easier to manage (McGowan & Sturman, 1996). In addition, they can also control the detection time of the kite at any altitude, which refers to the amount of time the kite spends in the same layer, and keep it stationary. Totems and Chazette (2016) validated a calibration method for a Raman lidar using a kite-carried humidity sensor. The calibration process is shown in Figure 8. In Figure 8b, the K_{WVMR} means a calibration constant. The ξ_{H_2O} and ξ_{N_2} are the Raman lidar overlap factors for water vapor and nitrogen, respectively. The $\Delta\tau(z)$ is the difference in total optical thickness between the two detection wavelengths of water vapor and nitrogen. $S_{H_2O}(z)$ and $S_{N_2}(z)$ are lidar signals for water vapor and nitrogen, respectively. When calibrating,

water vapor is measured simultaneously by kite ($r_{H_2O,kite}(z)$) and lidar ($r_{H_2O,lidar}(z)$), and the calibration function is represented by C(z). The K_{WVMR} is calculated using the calibration function. Guaranteeing the stable flight of the kite above the lidar site can greatly improve co-location coincidence for kite-based calibrations compared to radiosonde-based calibrations. This allows for the determination of overlap functions and calibration simultaneity factors. To verify its calibration capabilities, the WVMR profiles of the calibrated Raman lidar tests were compared with radiosondes measurements, satellite tests (Moderate-resolution Imaging Spectroradiometer, MODIS), ground-based sun photometer tests, and so on. Overall, the kite-based lidar calibration was found to be accurate and stable during the measurements. However, due to the increasing air traffic, the use of kites is limited not only by wind speed but also by strict local regulations.

With the development of the AErosol RObotic NETwork (AERONET), sun photometers have been widely applied for water vapor detection due to their affordability and ease of deployment (Ferrare et al., 2000; Ferrare et al., 2006; Pérez-Ramírez et al., 2014; Schmid et al., 2000). The calibration method for water vapor lidar based on a sun photometer has also emerged. Similar to other sensor-based calibration techniques, the calibration constant of lidar is determined by comparing data measured by a sun photometer and Raman lidar (Dai et al., 2018). The sun-photometer-based calibration technique was first reported by Vlăduţescu et al. (2007), but they did not provide detailed information about the method. To minimize the calibration error caused by the difference in atmospheric transmission varying extinction coefficients at two wavelengths (N_2 and H_2O channels), Dai et al. proposed a procedure for continuous calibration of Raman lidar, as shown in Figure 9. The Raman lidar was calibrated using the temperature and pressure profiles detected by co-located AERONET sun photometer observations and Global Data Assimilation System (GDAS) (Dai et al., 2018). The calibration results showed that the WVMR has a relative uncertainty of 11%.

Another external reference instrument is a microwave radiometer, which can provide high temporal resolution atmospheric water vapor data (Foth et al., 2015; Han et al., 1994; Hogg et al., 1983; Turner & Goldsmith, 1999). Limited by its low spatial resolution (Westwater et al., 2005), it is generally not used for lidar profile calibration. However, the integrated water vapor can be accurately detected. So microwave radiometer can be used for calibrating the vertical column concentration of water vapor (Foth et al., 2015).

3.1.2 | Internal calibration method and hybrid methods

In addition to the common external calibration methods that rely on other water vapor detection equipment, there were also internal calibration techniques that did not require an external reference instrument. The internal calibration is independent and constant, it can be found throughout the entire optical path in the lidar system. Theoretically, the uncertainty of all parameters in the system, such as the Raman cross-sections, the optical transmittance, the overlap factor, and the detectors'quantum efficiencies must be quantified and accounted for. Thanks to the homogeneous

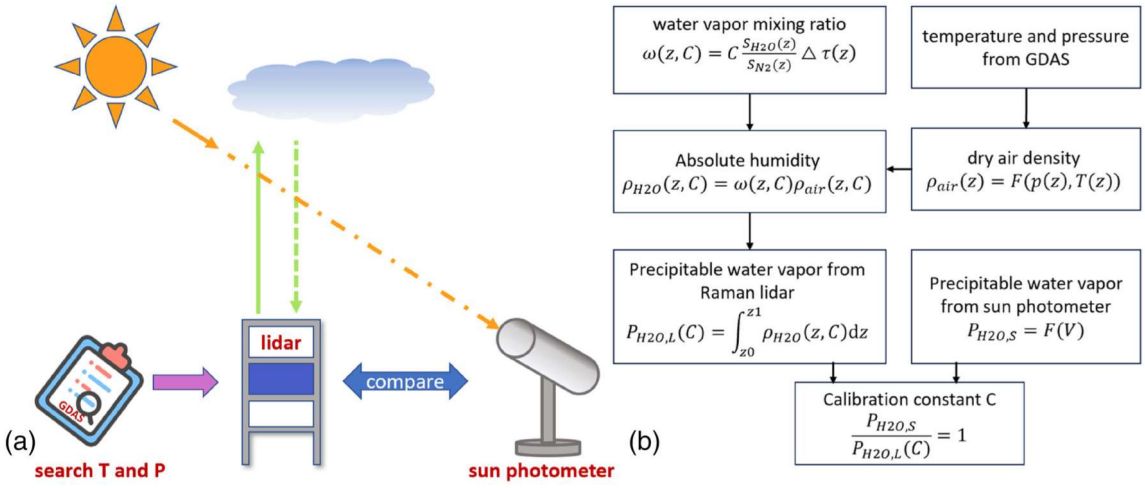

FIGURE 9 (a) Diagram of sun photometer-based calibration; (b) Flowchart of the sun photometer-based calibration procedure (Dai et al., 2018).

distribution of atmospheric nitrogen, its concentration is proportional to the mass of dry air. Therefore, the ratio of their densities is proportional to the WVMR (Whiteman et al., 1992). By using the ratio of optical efficiencies between the two Raman channels and the ratio of the Raman backscatter cross-sections of nitrogen and water vapor, Vaughan et al. (1988) and Leblanc et al. (2012) calculated the system calibration constant. However, the performance of the Raman lidar system may change over time, particularly the performance of the receiving unit, necessitating frequent repetition of this complex calibration process.

To obtain accurate efficiencies for each part of the system, diffuse sunlight or a standard lamp can be used as a light source to determine the lidar system calibration constant (Leblanc & McDermid, 2011; Vanessa Sherlock & Lenoble, 1999; Venable et al., 2011; Whiteman et al., 2011). This method used modeling of the incident light source or known spectral dependence to invert the measurements and infer T_{N_2}/T_{H_2O}. The effective cross-sections can be determined. The relative line strengths of the H_2O and N_2 at $\nu 1$ band can be calculated using semiempirical models. Line strengths can be normalized by the differential backscattering Raman cross-sections of the H_2O and N_2. The absolute cross-sections were obtained by convolving the Raman cross-section with the instrument function. Finally, the terms were combined again to evaluate the lidar calibration coefficient. Calibration of lidar using a lamp in front of the telescope has been proposed, enabling calibration without the need for routine use of radiosondes. In 1999, Sherlock et al. reported two light sources for lidar calibration: diffuse sunlight and a lamp. However, both of these sources proved difficult to use (Vanessa Sherlock & Lenoble, 1999) Figure 10.

The standard lamp-based calibration method can accurately measure changes in the change of calibration constant, but it cannot differentiate between spectral shifts caused by individual units or accurately identify the cause of the change. The uneven sampling of the lidar optics can lead to these errors. To solve these problems, Whiteman et al. used multiple lamps in different locations in front of the telescope to aid in the identification of atypical efficiency ratio measurements. Each lamp was run sequentially to record its intensity ratio as part of each "lamp calibration" exercise. (Whiteman et al., 2011). Venable et al. solved the above problem by employing a scanning lamp (Venable et al., 2011). The internal lamp-based calibration error was related to the filter band degrees, the lamp light intensity function, and the molecular cross-sections. Typically, the uncertainty in the molecular cross-sections was the most limiting factor (Penney & Lapp, 1976). There are many advantages to the lamp-based calibration method. However, it is impractical for some systems, such as lidars using large-aperture mirrors (Sica et al., 1995) or systems with multiple mirrors (Dinoev et al., 2013; Godin-Beekmann et al., 2003).

In 2008, a harsh calibration method was required to meet the measurement accuracy requirement of 5%–10% (Leblanc & McDermid, 2008). To achieve this goal, a calibration method combines absolute radiosonde-based calibration and standard lamp-based conventional (off-campaign) part calibration. This calibration method is shown in Figure 11. Occasional calibration campaigns based on radiosondes can be employed to obtain the averaged lidar constant (T_1 for campaign 1) and the corresponding averaged ratio (L_1 for campaign 1) of the water vapor and nitrogen channels based on the lamp. It can be assumed that this ratio remains constant over time. Then, without normalizing the standard lamp constant with a radiosonde, an absolute calibration of the water-vapor mixing ratio can be obtained by formulating. When this ratio slowly drifts over time, q_i needs to be calculated after campaign 2. In this case, L is no longer equal to L_1 and is replaced by L_i, which is the linear combination of L_1 and L_2. Benefiting from the reliable stability of the lamp-based calibration method and the availability of radiosonde, the calibrated Raman lidar has the potential for long-term observation of atmospheric water vapor.

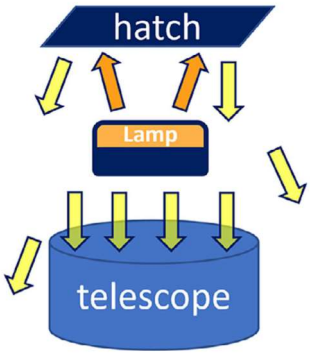

FIGURE 10 Diagram of standard lamp or diffuse sunlight-based lidar calibration.

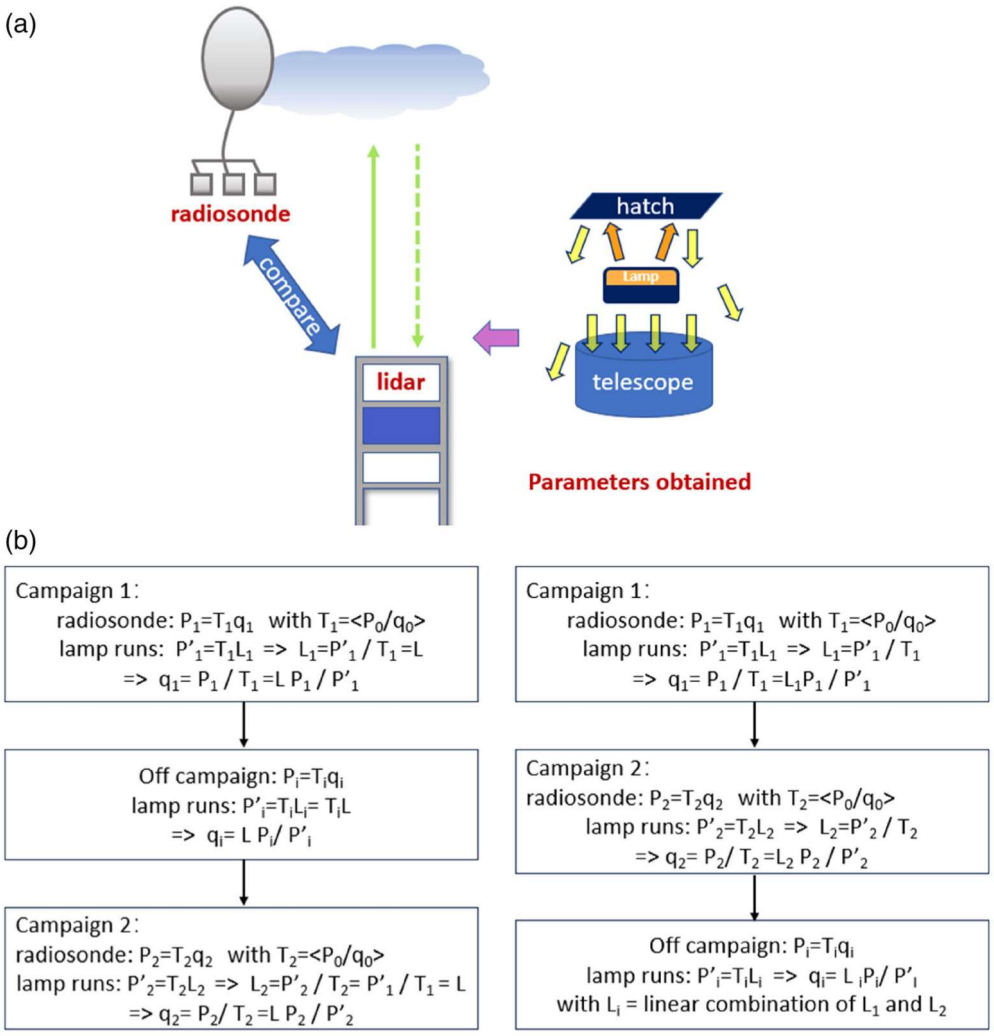

FIGURE 11 (a) Schematic of the integrated method based on radiosonde and lamp. (b) Schematic of the long-term water vapor Raman lidar calibration method (Leblanc & McDermid, 2008). P is the ratio of lidar signals (H_2O/N_2); T, q, P′, and L are the ratio of transmissions, water vapor mixing ratio, channel ratio during lamp runs, and ratio of lamp irradiances, respectively. <> means the mean of champaign.

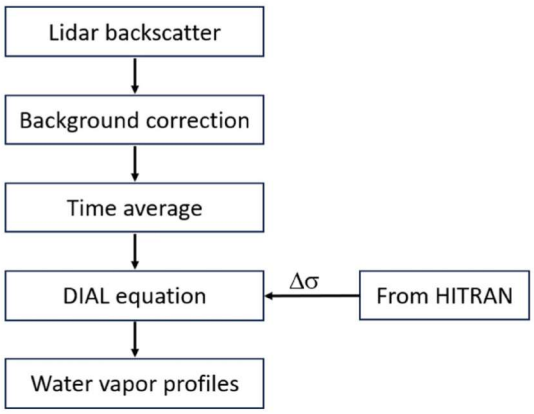

FIGURE 12 Flow chart of DIAL signal processing. $\Delta\sigma$ means the differential absorption cross-section.

In addition to the calibration techniques described above for the Raman lidar system, there are also other promising ways to calibrate the system, such as using satellite data (Filioglou et al., 2017), model data (Køltzow et al., 2017; Masson et al., 2011), a global positioning system (GPS) (David et al., 2017), and so forth.

3.2 | Calibration of DIAL lidar

3.2.1 | Based on database

As mentioned in Section 2, DIAL detection can self-calibrate. Only the absorption cross-sections when the wavelength is online and offline need to be known accurately. System calibration of DIAL involves the challenge of accurately determining the absorption cross-section. Therefore, one can directly obtain the differential absorption cross-section by querying the HITRAN database (Späth et al., 2016; Spuler et al., 2015), which allows the system to self-calibrate. The method of querying the database for self-calibration is the conventional method of differential absorption lidar is used for querying the database for self-calibration. This method can also be applied to other gas detection differential absorption lidar, such as CO_2 (Koch et al., 2008; Yu et al., 2017).

The data processing flow diagram of DIAL is shown in Figure 12. It can be seen that only the differential absorption section needs to be known to achieve the DIAL calibration. The water vapor profile will be obtained. The simplest way to obtain the differential absorption cross-section of water vapor is by directly searching the HITRAN database (Lsr et al., 2013; Wagner et al., 2013).

Temperature and pressure changes cause variations in the differential absorption cross-section. Therefore, temperature and pressure correction is required. In UHOH (University of Hohenheim), the whole DIAL signal processed flow is depicted in detail in Figure 13 (Späth et al., 2016). It can be seen from the flow chart that the system can realize self-calibration and only needs to input atmospheric parameters such as temperature, pressure, and the initial value of water vapor molecular number density. The temperature T(z) curve is obtained by querying the US Standard Atmosphere. The pressure profile, p(z), is determined by the surface value and temperature of the atmosphere. An initial value for the water vapor molecular number density, $N_{WV}(z)$, can also be obtained from the US Standard Atmosphere (Oceanographic & Noaa, 1976). The differential absorption cross-section can be obtained using HITRAN. During the UHOH, the calibrated DIAL participated in the Surface Atmosphere Boundary Layer Exchange (SABLE) campaign in southwestern Germany, successfully measuring water vapor layers in three dimensions.

3.2.2 | Based on the reference cell

For long-term measurements, the laser's wavelength may drift due to ambient temperature or other fluctuating factors. Therefore, laser wavelength stabilization is of concern in the DIAL technique (Fix et al., 2010). Furthermore, using the offline technique to determine the absorption cross-section based on the HITRAN database may result in measurement errors. Thus, obtaining the real-time absorption cross-section obtained is necessary for DIAL.

In 1995, NPL developed a facility to enable directly verify open-path measurement techniques (Milton et al., 1995). It is based on an open pass cell with a length of 10 m, and a diameter of 1 m, in which a gas with controlled different

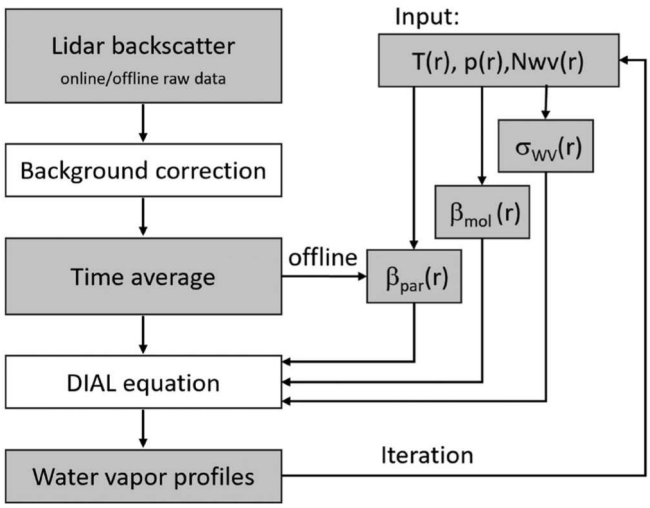

FIGURE 13 Flow chart of data processing (Späth et al., 2016).

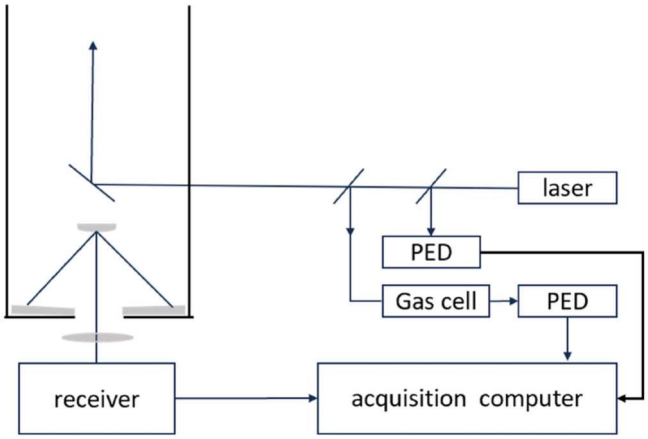

FIGURE 14 Schematic of the configuration and components for DIAL (Robinson et al., 2011). PED: two pyroelectric detectors.

TABLE 1 advantages and disadvantages of Raman lidar.

Advantages	Disadvantages
Low requirements for laser linewidth and stability	Difficulty in daytime detecting
Simple structure, robustness	Huge size
	Periodic calibration relies on external device

concentrations can be injected. By setting up this system within the appropriate proper range of the DIAL system and aligning the measurement line of sight through the aperture, it is possible to verify the concentration response and distance resolution of the system.

More than a decade later, NPL once again provided DIAL with the internal calibration technique. The whole system is depicted in Figure 14, and the output laser was divided into three beams (Robinson et al., 2011). The high-energy laser beam was directly sent to the atmosphere, while one of the low-energy beams was used to normalize the correlated return signals to offset any fluctuations in the output beam energy. Another low-energy laser beam was used to monitor in real-time the difference in absorption between the online and offline pulses as they passed through a gas cell containing a known quantity of gas. The equipment allows for the measurement of the absorption cross-section of the gas over time, which means the system can be self-calibrated.

In recent years, the development of lasers has led to the advancement of differential absorption lidar technology. However, this technology is still constrained by the demanding laser frequency stability requirements, making it challenging to achieve widespread application. Therefore, there are few reports on the calibration of differential absorption lidar for water vapor detection.

3.2.3 | Based on the external sensors

As mentioned in Section 3.1.1, calibration of the measurement is performed by using external sensors, which directly calibrate the entire system. It does not require determining the coefficients for each component of the lidar system, nor does it need to determine the uncertainty of the differential absorption cross-section. So this method is also suitable for DIAL systems. Although the external calibration method is also suitable for DIAL, it is usually implemented with a more convenient self-calibration method.

4 | SUMMARY AND RECOMMENDATIONS

In this review, the importance of atmospheric water detection and the conventional detection methods for its measurement were introduced. Moreover, the current status of the development of Raman lidar and DIAL technology was

described. Raman scattering is independent of the incident wavelength. Therefore, it requires less spectral purity of the transmitter and frequency stability of the receiver module. The advantages and disadvantages of Raman lidar are listed in Table 1. Raman scattering is not sensitive to wavelength, so Raman lidar has low requirements for laser linewidth and stability. The Raman lidar system has a simple structure, robustness, high detection accuracy, and high temporal and spatial resolution. It can realize unattended continuous observation and is suitable for a wide range of applications. However, due to its small Raman scattering cross-section, Raman lidar has limited capability for low detection during the daytime. Small Raman scattering cross-sections also require a high-energy laser transmitter, which results in a large system. The Raman lidar measurement provides a quantity proportional to the mixing ratio, rather than the water vapor concentration itself. This proportionality factor needs to be calibrated periodically to obtain accurate measurements.

The DIAL mechanism is based on elastic scattering, which has a much larger scattering cross-section than Raman scattering. This results in a high signal-to-noise ratio, enabling continuous daytime detection using low pulse energies. Therefore, for the same detection range, the DIAL system is smaller than the Raman lidar. Large scattered echoes are less affected by daytime background light, making daytime detection easier. DIAL has s self-calibration capability,

TABLE 2 Advantages and disadvantages of DIAL.

Advantages	Disadvantages
All-day detection	High requirements for laser linewidth and stability
Small size	Costly
Self-calibration	

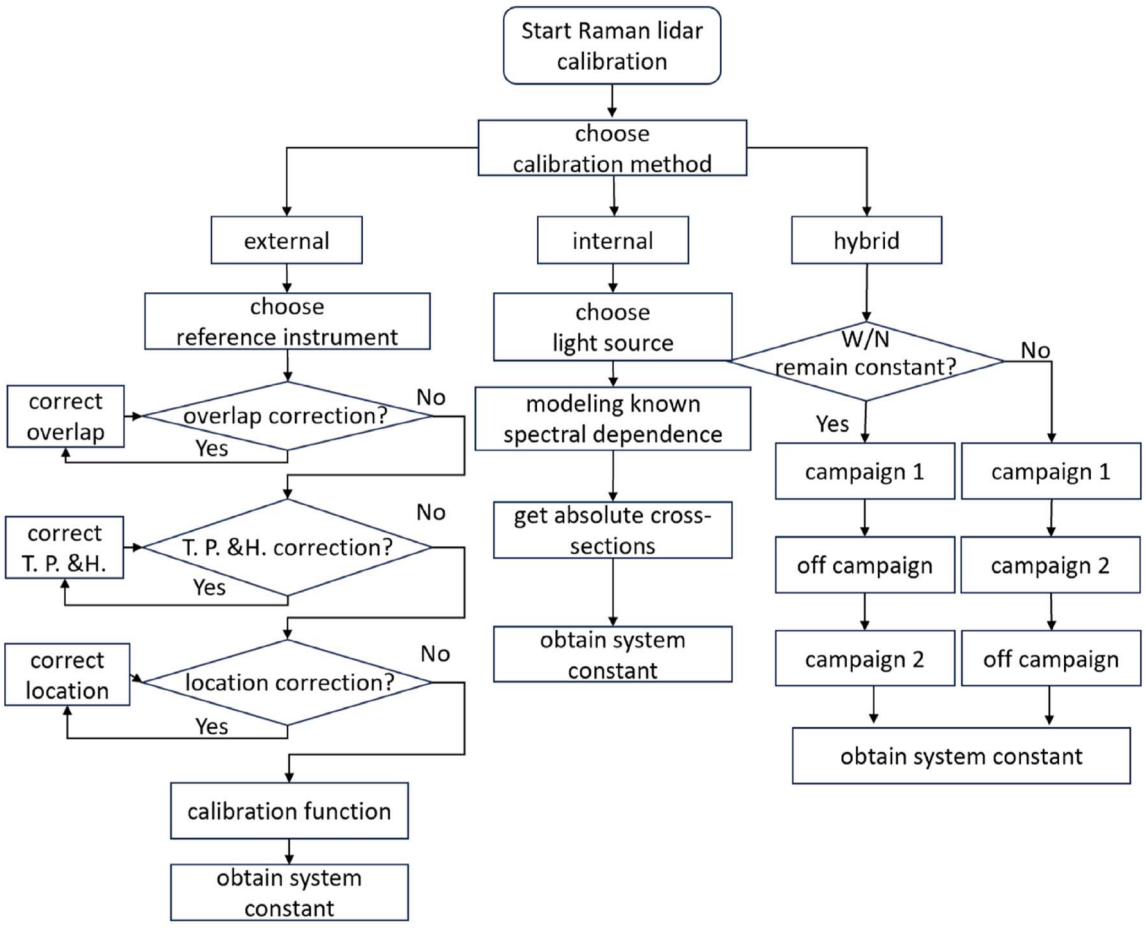

FIGURE 15 Flow chart of the Raman lidar calibration methods selection. T., P., and H. are temperature, pressure, and humidity, respectively. W/H means the averaged ratio of the water vapor and nitrogen channels based on the lamp.

which can be achieved by querying the database or using the built-in calibration module of the system. However, the water vapor absorption spectrum has a narrow linewidth, which necessitates the use of lasers with high-frequency stability. This results in high system costs. The advantages and disadvantages of DIAL are listed in Table 2.

This review provides a detailed description of the calibration principle of Raman lidar and various calibration methods. (1) The external calibration methods are based on other in situ measurement devices. (2) Internal calibration is performed using partial calibration data obtained from a lamp that emits a known spectrum. These calibration measurements are conducted on a regular schedule. (3) The hybrid of internal and external calibration methods. The flow chart for selecting the calibration method of lidar is shown in Figure 15. Radiosonde balloons, kite-type humidity sensors, and sun radiometers meet the above conditions and can be used as calibration instruments. For Raman lidar, the most commonly utilized method for external calibration is based on radiosonde. There is a partial overlap between the laser transmitter and receiver, resulting in a nonlinear relationship between the received power of the receiver and the concentration of gas. When there is a partial overlap between the transmitter and receiver, resulting in a nonlinear relationship between the received power and the gas concentration, overlap correction is required. In addition, a series of correction algorithms have been developed to account for the varying temperature, pressure, wind speed, and direction in each atmospheric layer. In addition, due to the commonly used external calibration method and comparison with radiosonde, the lidar may be far away, Hereto, a tracking method was proposed for position correction when the external calibration method is not feasible. In such cases, the internal calibration method can be applied. The internal calibration uses an incident light source or a known spectral dependence for modeling. The effective cross-section can be determined by measuring and inferring the ratio of nitrogen and water vapor channels. The relative line strength of H_2O and N_2 is calculated using a semi-empirical model. It is then normalized by the differential backscattered Raman cross-sections of H_2O and N_2. Recombine the terms to evaluate the lidar calibration coefficient. When neither external nor internal methods can meet the accuracy requirements, the hybrid method can be employed. Thanks to the advantages of the reliable stability of the lamp-based calibration method and the availability of radiosondes, there is potential to use this method to calibrate Raman lidar for long-term observation of atmospheric water vapor.

DIAL can also be calibrated by external devices. The external calibration process is similar to that of the Raman lidar. Self-calibration can be easily achieved by accurately determining the differential absorption cross-section at the specific differential absorption wavelength. Differential absorption cross-sections can be obtained directly through

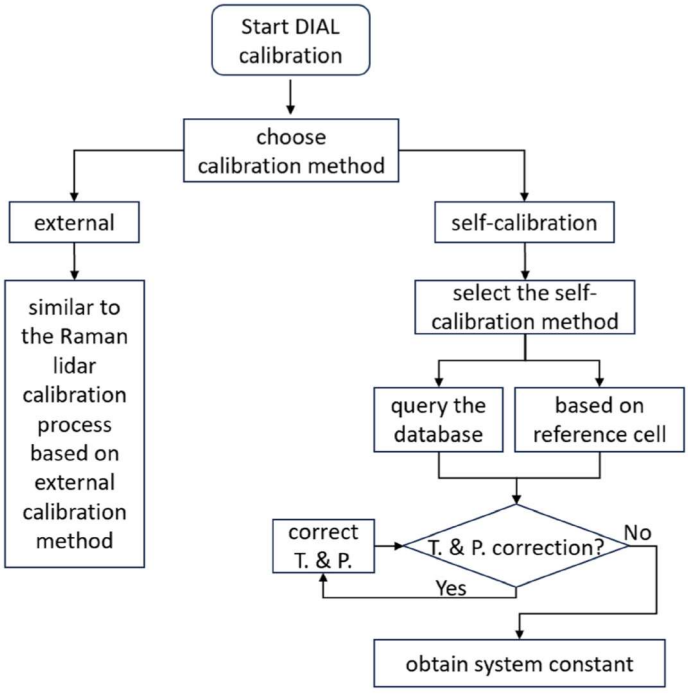

FIGURE 16 Flow chart of the DIAL calibration methods selection.

queries to the HITRAN database or by using a real-time detection reference cell. DIAL is usually implemented using the self-calibration method.

In our opinion, the future development of water vapor lidar detection and calibration can be expected.

1. Further improvement of the Raman lidar calibration.
   Atmosphere water vapor detection based on Raman lidar has matured and has obtained good detection results from various research groups in the world. Although many calibration methods have emerged to constantly optimize the system, it remains one of the main focuses of ongoing research. Moreover, a highly accurate and stable calibration mechanism will also make researchers more interested.
2. Further simplification of the DIAL system calibration mechanism Figure 16.
   Due to the narrow linewidth of the water vapor absorption spectral line, it is necessary to calibrate the wavelength of the system to ensure the stability of the laser wavelength during online/offline differential absorption testing. An external absorber cell is typically used for wavelength stabilization. However, even if the system has accurate wavelength calibration, in engineering applications such as operating in a long-term harsh environment, the laser's wavelength will still drift due to fluctuations in environmental factors such as temperature. To achieve a DIAL signal with high accuracy and stability, it is necessary to obtain the real-time absorption cross-section. The differential absorption cross-section of water vapor can be obtained in real-time using the same external gas cell. As a result, the DIAL water vapor lidar system can be self-calibrated. Simultaneously achieving wavelength stabilization and system calibration simplifies the complexity of the system.
3. Further rigorous error analysis.
   The direct HITRAN database query method used by DIAL does not account for the uncertainty caused by the drift of the actual absorption cross-section with laser wavelength. In addition, the calibration of the reference cell-based system depends on the concentrations of the sample gas in the cell. Such factors include temperature variations in the external environment, vibrations in the onboard system, bumps in the airborne system, and the effects of microgravity in the satellite-based system. Therefore, a rigorous error analysis is necessary.

Calibration is an essential process for detecting atmospheric water vapor using lidar. First of all, it is necessary to determine the type of lidar, and then select the calibration method based on its lidar type. There are two types of atmospheric water vapor lidar: Raman lidar and differential absorption lidar. The calibration methods of Raman lidar include the external calibration method, which relies on other equipment; the internal calibration method, which is based on the standard lamp; and the hybrid calibration method, which combines both internal and external calibration techniques. The calibration method based on external equipment requires the selection of suitable calibration equipment. High accuracy and high spatiotemporal resolution are the primary conditions for selection. Stable irradiance of standard lamps in the internal calibration method is a prerequisite for calibration. The calibration methods of DIAL include a unique self-calibration method and a commonly used calibration method based on external equipment. Accurate acquisition of differential absorption cross-sections is necessary for DIAL self-calibration.

AUTHOR CONTRIBUTIONS

Xinqian Guo: Investigation (equal); writing – original draft (equal). **Decheng wu:** Investigation (equal). **Zhenzhu wang:** Supervision (equal). **Bangxin Wang:** Writing – review and editing (equal). **Cheng li:** Validation (equal). **Qian deng:** Writing – review and editing (equal). **Dong liu:** Funding acquisition (equal); writing – review and editing (equal).

FUNDING INFORMATION

This research was supported by the Natural Science Foundation of Anhui Province (Grant No. 2208085UQ01); the Young Scientists Fund of the National Natural Science Foundation of China (Grant No. 42305142); the Open Fund of "Anhui Meteorological Detection Equipment Engineering Technology Research Center" (Grant No. 2023QXTC05); the Key Collaborative Research Program of the Alliance of International Science Organizations (Grant No. ANSO-CR-KP-2020-09); Hefei Research Institute Dean Fund Top Talents Cultivation Project (Grant No. BJPY2021A03); the HFIPS Director's Fund (Grant No. YZJJ202205-CX).

CONFLICT OF INTEREST STATEMENT

The authors declare that there is no conflict of interest.

DATA AVAILABILITY STATEMENT

Data sharing is not applicable to this article as no new data were created or analyzed in this study.

ORCID

Xinqian Guo https://orcid.org/0000-0002-0964-5126
Zhenzhu Wang https://orcid.org/0000-0002-3648-6124
Dong Liu https://orcid.org/0000-0002-1165-8233

RELATED WIREs ARTICLES

Estimating the spatial distribution of snow water equivalent in the world's mountains

Floating lidar as an advanced offshore wind speed measurement technique: Current technology status and gap analysis in regard to full maturity

REFERENCES

Adam, M., Demoz, B. B., Whiteman, D. N., Venable, D. D., Joseph, E., Gambacorta, A., Wei, J. C., Shephard, M. W., Miloshevich, L. M., Barnet, C. D., Herman, R. L., Fitzgibbon, J. E., & Connell, R. M. (2010). Water vapor measurements by Howard University Raman lidar during the WAVES 2006 campaign. *Journal of Atmospheric and Oceanic Technology*, *27*, 42–60.

Ansmann, A., Riebesell, M., Wandinger, U., Weitkamp, C., Voss, E., Lahmann, W., & Michaelis, W. (1992). Combined raman elastic-backscatter LIDAR for vertical profiling of moisture, aerosol extinction, backscatter, and LIDAR ratio. *Applied Physics B*, *55*(1), 18–28. https://doi.org/10.1007/BF00348608

Bruneau, D., Quaglia, P., Flamant, C., & Pelon, J. (2001). Airborne lidar LEANDRE II for water-vapor profiling in the troposphere. II. First results. *Applied Optics*, *40*(21), 3462–3475. https://doi.org/10.1364/ao.40.003462

Chazette, P., Marnas, F., & Totems, J. (2014). The mobile water vapor aerosol Raman LIdar and its implication in the framework of the HyMeX and ChArMEx programs: Application to a dust transport process. *Atmospheric Measurement Techniques*, *7*(6), 1629–1647. https://doi.org/10.5194/amt-7-1629-2014

Collis, R., & Russell, P. B. (1976). *Lidar measurement of particles and gases by elastic backscattering and differential absorption*. Springer.

Cooney, J. (1969). Remote measurements of atmospheric water vapor profiles using the Raman component of laser backscatter. *Journal of Applied Meteorology*, *9*(1), 182–184.

Dai, G., Althausen, D., Hofer, J., Engelmann, R., Seifert, P., Bühl, J., Mamouri, R.-E., Wu, S., & Ansmann, A. (2018). Calibration of Raman lidar water vapor profiles by means of AERONET photometer observations and GDAS meteorological data. *Atmospheric Measurement Techniques*, *11*(5), 2735–2748. https://doi.org/10.5194/amt-11-2735-2018

David, L., Bock, O., Thom, C., Bosser, P., & Pelon, J. (2017). Study and mitigation of calibration factor instabilities in a water vapor Raman lidar. *Atmospheric Measurement Techniques*, *10*(7), 2745–2758. https://doi.org/10.5194/amt-10-2745-2017

Dinoev, T., Simeonov, V., Arshinov, Y., Bobrovnikov, S., Ristori, P., Calpini, B., Parlange, M., & van den Bergh, H. (2013). Raman lidar for meteorological observations, RALMO – Part 1: Instrument description. *Atmospheric Measurement Techniques*, *6*(5), 1329–1346. https://doi.org/10.5194/amt-6-1329-2013

Dirksen, R. J., Sommer, M., Immler, F. J., Hurst, D. F., Kivi, R., & Vömel, H. (2014). Reference quality upper-air measurements: GRUAN data processing for the Vaisala RS92 radiosonde. *Atmospheric Measurement Techniques*, *7*(12), 4463–4490. https://doi.org/10.5194/amt-7-4463-2014

Ferrare, R., Ismail, S., Browell, E., Brackett, V., Clayton, M., Kooi, S., Melfi, S. H., Whiteman, D., Schwemmer, G., Evans, K., Russell, P., Livingston, J., Schmid, B., Holben, B., Remer, L., Smirnov, A., & Hobbs, P. V. (2000). Comparison of aerosol optical properties and water vapor among ground and airborne lidars and sun photometers during TARFOX. *Journal of Geophysical Research: Atmospheres*, *105*(D8), 9917–9933. https://doi.org/10.1029/1999jd901202

Ferrare, R., Turner, D., Clayton, M., Schmid, B., Redemann, J., Covert, D., Elleman, R., Ogren, J., Andrews, E., Goldsmith, J. E. M., & Jonsson, H. (2006). Evaluation of daytime measurements of aerosols and water vapor made by an operational Raman lidar over the southern Great Plains. *Journal of Geophysical Research*, *111*(D5), D05S08. https://doi.org/10.1029/2005jd005836

Ferrare, R. A., Browell, E. V., Ismail, S., Kooi, S. A., Brasseur, L. H., Brackett, V. G., Clayton, M. B., Barrick, J. D. W., Diskin, G. S., Goldsmith, J. E. M., Lesht, B. M., Podolske, J. R., Sachse, G. W., Schmidlin, F. J., Turner, D. D., Whiteman, D. N., Tobin, D., Miloshevich, L. M., Revercomb, H. E., ... Di Girolamo, P. (2004). Characterization of upper-troposphere water vapor measurements during AFWEX using LASE. *Journal of Atmospheric and Oceanic Technology*, *21*(12), 1790–1808. https://doi.org/10.1175/jtech-1652.1

Ferrare, R. A., Melfi, S. H., Whiteman, D. N., Evans, K. D., & Starr, D. O. C. (1995). A comparison of water vapor measurements made by Raman lidar and radiosondes. *Journal of Atmospheric & Oceanic Technology*, *12*(6), 1177–1195.

Filioglou, M., Nikandrova, A., Niemelä, S., Baars, H., Mielonen, T., Leskinen, A., Brus, D., Romakkaniemi, S., Giannakaki, E., & Komppula, M. (2017). Profiling water vapor mixing ratios in Finland by means of a Raman lidar, a satellite and a model. *Atmospheric Measurement Techniques*, *10*(11), 4303–4316. https://doi.org/10.5194/amt-10-4303-2017

Fix, A., Ehret, G., Löhring, J., Hoffmann, D., & Alpers, M. (2010). Water vapor differential absorption lidar measurements using a diode-pumped all-solid-state laser at 935 nm. *Applied Physics B*, *102*(4), 905–915. https://doi.org/10.1007/s00340-010-4310-5

Foth, A., Baars, H., Di Girolamo, P., & Pospichal, B. (2015). Water vapour profiles from Raman lidar automatically calibrated by microwave radiometer data during HOPE. *Atmospheric Chemistry and Physics*, *15*(5), 7753–7763.

Godin-Beekmann, S., Porteneuve, J., & Garnier, A. (2003). Systematic DIAL lidar monitoring of the stratospheric ozone vertical distribution at observatoire de haute-Provence (43.92 degrees N, 5.71 degrees E). *Journal of Environmental Monitoring*, *5*(1), 57–67. https://doi.org/10.1039/b205880d

Guichard, F., Parsons, D., & Miller, E. (2000). Thermodynamic and radiative impact of the correction of sounding humidity bias in the tropics. *Journal of Climate*, *13*(20), 3611–3624. https://doi.org/10.1175/1520-0442(2000)013<3611:Tariot>2.0.Co;2

Han, Y., Snider, J. B., Westwater, E. R., Melfi, S. H., & Ferrare, R. A. (1994). Observations of water vapor by ground-based microwave radiometers and Raman lidar. *Journal of Geophysical Research Atmospheres*, *99*(D9), 18695–18702.

He, Y., Yi, F., Liu, F., Yin, Z., & Zhou, J. (2022). Ice nucleation of cirrus clouds related to the transported dust layer observed by ground-based lidars over Wuhan, China. *Advances in Atmospheric Sciences*, *39*(12), 2071–2086. https://doi.org/10.1007/s00376-021-1192-x

Hicks-Jalali, S., Sica, R. J., Haefele, A., & Martucci, G. (2019). Calibration of a water vapour Raman lidar using GRUAN-certified radiosondes and a new trajectory method. *Atmospheric Measurement Techniques*, *12*(7), 3699-3716. https://doi.org/10.5194/amt-2018-246

Hogg, D. C., Guiraud, F. O., Snider, J. B., Decker, M. T., & Westwater, E. R. (1983). A steerable Dual-Channel microwave radiometer for measurement of water vapor and liquid in the troposphere. *Journal of Applied Meteorology*, *22*(5), 789–806.

Immler, F. J., Dykema, J., Gardiner, T., Whiteman, D. N., Thorne, P. W., & Vömel, H. (2010). Reference quality upper-air measurements: Guidance for developing GRUAN data products. *Atmospheric Measurement Techniques*, *3*(5), 1217–1231. https://doi.org/10.5194/amt-3-1217-2010

Koch, G. J., Beyon, J. Y., Gibert, F., Barnes, B. W., Ismail, S., Petros, M., Petzar, P. J., Yu, J., Modlin, E. A., & Davis, K. J. (2008). Side-line tunable laser transmitter for differential absorption lidar measurements of CO2: Design and application to atmospheric measurements. *Applied Optics*, *47*(7), 944–956.

Køltzow, M. Ø., Yang, X., Toll, V., Tijm, S., Subias, A., Muñoz, D. S., Samuelsson, P., Rontu, L., Onvlee, J., Nielsen, K. P., Niemelä, S., Lenderink, G., Ivarsson, K.-I., Hortal, M., Homleid, M., Hansen-Sass, B., Gleeson, E., de Rooy, W., Calvo, J., ... Bengtsson, L. (2017). The HARMONIE–AROME model configuration in the ALADIN–HIRLAM NWP system. *Monthly Weather Review*, *145*(5), 1919–1935. https://doi.org/10.1175/mwr-d-16-0417.1

Kulla, B., & Ritter, C. (2019). Water vapor calibration: Using a Raman lidar and Radiosoundings to obtain highly resolved water vapor profiles. *Remote Sensing*, *11*(6), 616. https://doi.org/10.3390/rs11060616

Leblanc, T., & McDermid, I. S. (2008). Accuracy of Raman lidar water vapor calibration and its applicability to long-term measurements. *Applied Optics*, *47*(30), 5592–5603.

Leblanc, T., & McDermid, I. S. (2011). Reply to "comments on accuracy of Raman lidar water vapor calibration and its applicability to long-term measurements" by Whiteman et al. *Applied Optics*, *50*(15), 2177–2178. https://doi.org/10.1364/AO.50.002177

Leblanc, T., McDermid, I. S., & Walsh, T. D. (2012). Ground-based water vapor raman lidar measurements up to the upper troposphere and lower stratosphere for long-term monitoring. *Atmospheric Measurement Techniques*, *5*(1), 17–36. https://doi.org/10.5194/amt-5-17-2012

Lsr, A., Ieg, A., Yb, B., Ab, C., Dcb, D., Pfb, E., Mb, F., Lb, G., Vb, H., & Lrb, I. (2013). The HITRAN2012 molecular spectroscopic database. *Journal of Quantitative Spectroscopy and Radiative Transfer*, *130*, 4–50.

Lu, D., Pan, W., & Wang, Y. (2018). Atmospheric profiling synthetic observation system in Tibet. *Advances in Atmospheric Sciences*, *35*(3), 264–267. https://doi.org/10.1007/s00376-017-7251-7

Madonna, F., Amodeo, A., Boselli, A., Cornacchia, C., Cuomo, V., D'Amico, G., Giunta, A., Mona, L., & Pappalardo, G. (2011). CIAO: The CNR-IMAA advanced observatory for atmospheric research. *Atmospheric Measurement Techniques*, *4*(6), 1191–1208. https://doi.org/10.5194/amt-4-1191-2011

Masson, V., Lac, C., Bouttier, F., Bénard, P., Hello, G., Malardel, S., Brousseau, P., & Seity, Y. (2011). The AROME-France convective-scale operational model. *Monthly Weather Review*, *139*(3), 976–991. https://doi.org/10.1175/2010mwr3425.1

Mattis, I., Ansmann, A., Althausen, D., Jaenisch, V., Wandinger, U., Müller, D., Arshinov, Y. F., Bobrovnikov, S. M., & Serikov, I. B. (2002). Relative-humidity profiling in the troposphere with a Raman lidar. *Applied Optics*, *41*(30), 6451–6462. https://doi.org/10.1364/AO.41.006451

Mazany, R. A., Businger, S., Gutman, S. I., & Roeder, W. (2002). A lightning prediction index that utilizes GPS integrated precipitable water vapor. *Weather and Forecasting*, *17*(5), 1034–1047.

McGowan, H. A., & Sturman, A. P. (1996). A kite based atmospheric sounding system. *Boundary-Layer Meteorology*, *77*(3–4), 395–399. https://doi.org/10.1007/bf00123534

Melfi, S. H. (1972). Remote measurements of the atmosphere using Raman scattering. *Applied Optics*, *11*(7), 1605.

Melfi, S. H., Lawrence, J. D., & Mccormick, M. P. (1969). Observation of raman scattering by water vapor in the atmosphere. *Applied Physics Letters*, *15*(9), 295–297.

Miloshevich, L. M., Paukkunen, A., Vömel, H., & Oltmans, S. J. (2004). Development and validation of a time-lag correction for Vaisala radiosonde humidity measurements. *Journal of Atmospheric and Oceanic Technology*, *21*(9), 1305–1327. https://doi.org/10.1175/1520-0426(2004)021<1305:davoat>2.0.co;2

Miloshevich, L. M., Vömel, H., Whiteman, D. N., & Leblanc, T. (2009). Accuracy assessment and correction of Vaisala RS92 radiosonde water vapor measurements. *Journal of Geophysical Research*, *114*(D11), D11305. https://doi.org/10.1029/2008jd011565

Milton, M., Woods, P. T., Partridge, R. H., & Goody, B. A. (1995). *Calibration of DIAL and open-path systems using external gas cells*. International Society for Optics and Photonics.

Moss, A., Sica, R. J., McCullough, E., Strawbridge, K., Walker, K., & Drummond, J. (2013). Calibration and validation of water vapour lidar measurements from Eureka, Nunavut, using radiosondes and the atmospheric chemistry experiment Fourier transform spectrometer. *Atmospheric Measurement Techniques*, *6*, 741–749. https://doi.org/10.5194/amtd-5-5665-2012

Oceanographic, N., & Noaa, A. A. (1976). U.S. Standard Atmosphere.

Penney, C. M., & Lapp, M. (1976). Raman-scattering cross sections for water vapor. *Journal of the Optical Society of America*, *66*(5), 422–425. https://doi.org/10.1364/JOSA.66.000422

Pérez-Ramírez, D., Whiteman, D. N., Smirnov, A., Lyamani, H., Holben, B. N., Pinker, R., Andrade, M., & Alados-Arboledas, L. (2014). Evaluation of AERONET precipitable water vapor versus microwave radiometry, GPS, and radiosondes at ARM sites. *Journal of Geophysical Research: Atmospheres*, *119*(15), 9596–9613. https://doi.org/10.1002/2014jd021730

Reiche, M., Funk, R., Zhang, Z., Hoffmann, C., Li, Y., & Sommer, M. (2012). Using a parafoil kite for measurement of variations in particulate matter—A kite-based dust profiling approach. *Atmospheric and Climate Sciences*, *2*(1), 41–51. https://doi.org/10.4236/acs.2012.21006

Robinson, R., Gardiner, T., Innocenti, F., Woods, P., & Coleman, M. (2011). Infrared differential absorption lidar (DIAL) measurements of hydrocarbon emissions. *Journal of Environmental Monitoring*, *13*(8), 2213–2220. https://doi.org/10.1039/c0em00312c

Sandeep, A., Rao, T. N., & Rao, S. V. B. (2015). A comprehensive investigation on afternoon transition of the atmospheric boundary layer over a tropical rural site. *Atmospheric Chemistry and Physics*, *15*(13), 7605–7617. https://doi.org/10.5194/acp-15-7605-2015

Schmid, B., Livingston, J. M., Russell, P. B., Durkee, P. A., Jonsson, H. H., Collins, D. R., Flagan, R. C., Seinfeld, J. H., Gassó, S., Hegg, D. A., Öström, E., Noone, K. J., Welton, E. J., Voss, K. J., Gordon, H. R., Formenti, P., & Andreae, M. O. (2000). Clear-sky closure studies of lower tropospheric aerosol and water vapor during ACE-2 using airborne sunphotometer, airborne in-situ, space-borne, and ground-based measurements. *Tellus B: Chemical and Physical Meteorology*, *52*(2), 568. https://doi.org/10.3402/tellusb.v52i2.16659

Seidel, D. J., Berger, F. H., Diamond, H. J., Dykema, J., Goodrich, D., Immler, F., Murray, W., Peterson, T., Sisterson, D., Sommer, M., Thorne, P., Vomel, H., & Wang, J. (2009). Reference upper-air observations for climate: Rationale, progress, and plans. *Bulletin of the American Meteorological Society*, *90*(3), 361–369. https://doi.org/10.1175/2008bams2540.1

Shine, K. P., & Sinha, A. (1991). Sensitivity of the Earth's climate to height-dependent changes in the water vapour mixing ratio. *Nature*, *354*(6352), 382–384. https://doi.org/10.1038/354382a0

Sica, R. J., Sargoytchev, S., Argall, P. S., Borra, E. F., Girard, L., Sparrow, C. T., & Flatt, S. (1995). Lidar measurements taken with a large-aperture liquid mirror. 1. Rayleigh-scatter system. *Applied Optics*, *34*(30), 6925–6936. https://doi.org/10.1364/AO.34.006925

Späth, F., Behrendt, A., Muppa, S. K., Metzendorf, S., Riede, A., & Wulfmeyer, V. (2016). 3-D water vapor field in the atmospheric boundary layer observed with scanning differential absorption lidar. *Atmospheric Measurement Techniques*, *9*(4), 1701–1720. https://doi.org/10.5194/amt-9-1701-2016

Spuler, S. M., Repasky, K. S., Morley, B., Moen, D., Hayman, M., & Nehrir, A. R. (2015). Field-deployable diode-laser-based differential absorption lidar (DIAL) for profiling water vapor. *Atmospheric Measurement Techniques*, *8*(3), 1073–1087. https://doi.org/10.5194/amt-8-1073-2015

Totems, J., & Chazette, P. (2016). Calibration of a water vapour Raman lidar with a kite-based humidity sensor. *Atmospheric Measurement Techniques*, *9*(3), 1083–1094. https://doi.org/10.5194/amt-9-1083-2016

Turner, D. D., & Goldsmith, J. E. M. (1999). Twenty-four-hour Raman lidar water vapor measurements during the atmospheric radiation measurement program's 1996 and 1997 water vapor intensive observation periods. *Journal of Atmospheric and Oceanic Technology*, *16*(8), 1062–1076. https://doi.org/10.1175/1520-0426(1999)016<1062:tfhrlw>2.0.co;2

Turner, D. D., Lesht, B. M., Clough, S. A., Liljegren, J. C., Revercomb, H. E., & Tobin, D. C. (2003). Dry bias and variability in Vaisala RS80-H radiosondes: The ARM experience. *Journal of Atmospheric and Oceanic Technology*, *20*(1), 117–132.

Vanessa Sherlock, A. H., & Lenoble, J. (1999). Methodology for the independent calibration of Raman backscatter water-vapor lidar systems. *Applied Optics*, *38*(27), 5816.

Vaughan, G., Wareing, D., Thomas, L., & Mitev, V. (1988). Humidity measurements in the free troposphere using Raman backscatter. *Quarterly Journal of the Royal Meteorological Society*, *114*, 1471–1484.

Venable, D. D., Whiteman, D. N., Calhoun, M. N., Dirisu, A. O., Connell, R. M., & Landulfo, E. (2011). Lamp mapping technique for independent determination of the water vapor mixing ratio calibration factor for a Raman lidar system. *Applied Optics*, *50*(23), 4622–4632.

Vlăduţescu, D. V., Wu, Y., Charles, L., Gross, B. M., Moshary, F., & Ahmed, S. A. (2007). Analyses of Raman lidar calibration techniques based on water vapor mixing ratio measurements.

Wagner, G., Behrendt, A., Wulfmeyer, V., Spath, F., & Schiller, M. (2013). High-power Ti:Sapphire laser at 820 nm for scanning ground-based water-vapor differential absorption lidar. *Applied Optics*, *52*(11), 2454–2469. https://doi.org/10.1364/AO.52.002454

Weitkamp, C. (2006). *Lidar: Range-resolved optical remote sensing of the atmosphere* (Vol. 102). Springer Science & Business.

Westwater, E. R., Crewell, S., Mätzler, C., & Cimini, D. (2005). Principles of surface-based microwave and millimeter wave radiometric remote sensing of the troposphere. *Quad Soc Ital Elettromagnetismo*, *1*(3), 50–90.

Whiteman, D. N. (2003a). Examination of the traditional Raman lidar technique. I. Evaluating the temperature-dependent lidar equations. *Applied Optics*, *42*(15), 2571–2592.

Whiteman, D. N. (2003b). Examination of the traditional Raman lidar technique. II. Evaluating the ratios for water vapor and aerosols. *Applied Optics*, *42*(15), 2593–2608.

Whiteman, D. N., Demoz, B., Rush, K., Schwemmer, G., Gentry, B., Di Girolamo, P., Comer, J., Veselovskii, I., Evans, K., Melfi, S. H., Wang, Z., Cadirola, M., Mielke, B., Venable, D., & van Hove, T. (2006). Raman lidar measurements during the international H_2O project. Part I: Instrumentation and analysis techniques. *Journal of Atmospheric and Oceanic Technology*, *23*(2), 157–169. https://doi.org/10.1175/jtech1838.1

Whiteman, D. N., Melfi, S. H., & Ferrare, R. A. (1992). Raman lidar system for the measurement of water vapor and aerosols in the Earth's atmosphere. *Applied Optics*, *31*(16), 3068–3082. https://doi.org/10.1364/AO.31.003068

Whiteman, D. N., Russo, F., Demoz, B., Miloshevich, L. M., Veselovskii, I., Hannon, S., Wang, Z., Vömel, H., Schmidlin, F., Lesht, B., Moore, P. J., Beebe, A. S., Gambacorta, A., & Barnet, C. (2006). Analysis of Raman lidar and radiosonde measurements from the AWEX-G field campaign and its relation to aqua validation. *Journal of Geophysical Research*, *111*(D9), D09S09. https://doi.org/10.1029/2005jd006429

Whiteman, D. N., Venable, D., & Landulfo, E. (2011). Comments on "Accuracy of Raman lidar water vapor calibration and its applicability to long-term measurements". *Applied Optics*, *50*(15), 2170–2176.

Wulfmeyer, V., & Bösenberg, J. (1998). Ground-based differential absorption lidar for water-vapor profiling: Assessment of accuracy, resolution, and meteorological applications. *Applied Optics*, *37*(18), 3825–3844. https://doi.org/10.1364/AO.37.003825

Yu, J., Petros, M., Singh, U. N., Refaat, T. F., Reithmaier, K., Remus, R. G., & Johnson, W. (2017). An airborne 2-μm double-pulsed direct-detection lidar instrument for atmospheric CO2 column measurements. *Journal of Atmospheric and Oceanic Technology*, *34*(2), 385–400. https://doi.org/10.1175/jtech-d-16-0112.1

How to cite this article: Guo, X., Wu, D., Wang, Z., Wang, B., Li, C., Deng, Q., & Liu, D. (2023). A review of atmospheric water vapor lidar calibration methods. *WIREs Water*, e1712. https://doi.org/10.1002/wat2.1712